

[C II] Haloes in ALPINE galaxies: smoking-gun of galactic outflows?

E. Pizzati ^{1,2}★ A. Ferrara,¹ A. Pallottini ¹ L. Sommovigo ¹ M. Kohandel ¹ and S. Carniani ¹

¹*Scuola Normale Superiore, Piazza dei Cavalieri 7, I-56126 Pisa, Italy*

²*Leiden Observatory, Leiden University, PO Box 9513, NL-2300 RA Leiden, the Netherlands*

Accepted 2022 December 15. Received 2022 December 15; in original form 2022 August 2

ABSTRACT

ALMA observations have revealed that many high-redshift galaxies are surrounded by extended (10–15 kpc) [C II]-emitting haloes that are not predicted by even the most advanced zoom-in simulations. Using a semi-analytical model, in a previous work we suggested that such haloes are produced by starburst-driven, catastrophically cooling outflows. Here, we further improve the model and compare its predictions with data from seven star-forming ($10 \lesssim \text{SFR}/M_{\odot} \text{ yr}^{-1} \lesssim 100$) galaxies at $z = 4\text{--}6$, observed in the ALPINE survey. We find that (a) detected [C II] haloes are a natural by-product of starburst-driven outflows; (b) the outflow mass loading factors are in the range $4 \lesssim \eta \lesssim 7$, with higher η values for lower mass, lower star formation rate systems, and scale with stellar mass as $\eta \propto M_{*}^{-0.43}$, consistently with the momentum-driven hypothesis. Our model suggests that outflows are widespread phenomena in high- z galaxies. However, in low-mass systems the halo extended [C II] emission is likely too faint to be detected with the current levels of sensitivity.

Key words: (photodissociation region (PDR) – galaxies: high-redshift – galaxies: ISM.

1 INTRODUCTION

Investigating the complex environments of galaxies at the end of the Epoch of Reionization (EoR; redshift $z \gtrsim 5.5$; for recent reviews, see Dayal & Ferrara 2018; Hodge & da Cunha 2020) is one of the most pressing research goals of modern astrophysics. As shown by cosmological simulations (Hopkins et al. 2018; Vogelsberger et al. 2020; Katz et al. 2021; Pallottini et al. 2022), galaxies at the EoR show different properties with respect to the ones seen in the local Universe [e.g. smaller sizes, higher specific star formation rates (SFRs), and warmer dust].

In the last few years, astounding progress has been made in detecting primordial galaxies up to $z \sim 13$ (Oesch et al. 2012; Harikane et al. 2022). This has fuelled a strong and widespread interest in detailed studies of their internal structure. As a result, these early systems are now being routinely identified in large-scale optical/near-infrared (NIR) surveys (Bacon et al. 2017; Bouwens et al. 2015), and targeted interferometric observations at far-infrared (FIR) wavelengths (Le Fèvre et al. 2020; Bouwens et al. 2022).

Specifically, the *Hubble Space Telescope* (HST) measured sizes and morphological properties of high-redshift galaxies at rest-frame ultraviolet (UV) wavelengths (Oesch et al. 2009; Shibuya, Ouchi & Harikane 2015; Bradley et al. 2014; Bouwens et al. 2015; Oesch et al. 2016; Bouwens et al. 2017; Livermore, Finkelstein & Lotz 2017; Kawamata et al. 2018). These studies successfully characterized the evolution of the rest-frame galaxy UV luminosity functions (LFs), star formation, stellar build-up history, and size growth, giving a first statistical characterization of galactic systems up to $z \approx 10$.

At the same time, the appearances of the Atacama Large Millimeter/submillimeter Array (ALMA) and the NOthern Extended Millimeter Array (NOEMA) have opened a new window on the primordial Universe, exploring the obscured star formation and interstellar medium (ISM) line emission at rest-frame FIR wavelengths up to $z \approx 13$ (Harikane et al. 2022). Combining the information coming from the dust continuum emission, as well as from some relevant FIR emission lines such as [C II] 158 μm , [O III] 88 μm , and CO from various rotational levels, several works studied the internal properties of galaxies, such as their assembly history, ISM thermal structure, gas dynamics, dust/metal enrichment, and interstellar radiation field (ISRF; Maiolino et al. 2015; Capak et al. 2015; Pentericci et al. 2016; Matthee et al. 2017; Carniani et al. 2018; Gallerani et al. 2018; Hashimoto et al. 2018; Carniani et al. 2020; Calura et al. 2021).

In particular, the [C II] ${}^2P_{3/2} \rightarrow {}^2P_{1/2}$ fine-structure transition has been the workhorse for many observational and theoretical endeavours. Due to its brightness and ubiquity (it traces many different phases of the ISM, e.g. Stacey et al. 1991; Hollenbach & Tielens 1999; Wolfire et al. 2003), this line can provide essential information on the physics of galaxies at high redshift (e.g. Vallini et al. 2015; Olsen et al. 2017). For instance, different works have focused on interpreting the local [C II]–SFR relation (De Looze et al. 2014; Herrera-Camus et al. 2015, 2018) in the context of early systems (Carniani et al. 2018; Carniani et al. 2020; Schaerer et al. 2020), studying its dependence on the burstiness of the star formation process, the gas density, and the intensity of the ISRF (Ferrara et al. 2019; Pallottini et al. 2019; Vallini et al. 2021).

A key result that emerged thanks to spatially resolved observations of the [C II] line is the existence of *extended* [C II] haloes around normal, star-forming galaxies at high redshift (Fujimoto et al. 2019; Fujimoto et al. 2020; Ginolfi et al. 2020; Herrera-Camus et al. 2021; Akins et al. 2022; Fudamoto et al. 2022). These haloes imply

* E-mail: pizzati@strw.leidenuniv.nl

the presence of singly ionized carbon extending out to distances significantly larger than the size of galactic discs.

The first evidence for such haloes was obtained by Fujimoto et al. (2019) who stacked ALMA observations of 18 main-sequence galaxies at redshifts $z = 5-7$ directly in the uv-visibility plane. The data have revealed the presence of a [C II] surface brightness $\approx 5 \times$ times more extended than the *HST* stellar continuum and ALMA dust continuum maps. This implies the presence of a carbon halo extending out to ≈ 10 kpc from the stacked galaxy centre (i.e. well into the circumgalactic medium of these galaxies).

This early result was then backed up by detailed observations within the ALMA ALPINE Large Program (B  thermin et al. 2020; Faisst et al. 2020; Le F  vre et al. 2020). This programme opened up for the first time the possibility of studying extended haloes around normal, high-redshift galaxies at the individual level. Fujimoto et al. (2020, hereafter F20) measured the physical extent of [C II] line-emitting gas in 23 star-forming galaxies at $z = 4-6$. This study found that, in the vast majority of cases, the size of the [C II] emitting region exceeds the size of the UV stellar continuum by factors of $\sim 2-3$, and concluded that at least ~ 30 per cent of the sources have a [C II] halo extending over ten-kpc scales. Interestingly, the authors studied also the dependence of the size of this extended [C II] line structure on few galactic properties, finding a positive correlation with e.g. star-formation rate (SFR) and stellar mass. Follow-up observations are needed to test whether [C II] haloes are a universal feature in high-redshift star-forming galaxies, and to investigate the observed spread in the haloes size and morphology.

On top of these findings, observations of SPD.81, a $z \approx 3$ gravitationally lensed dusty star-forming galaxy, showed that ~ 50 per cent of [C II] emission arises in the external (i.e. not FIR-bright) region of the galaxy (Rybak et al. 2019). Another interesting result came from deep observations of HZ4, a typical star-forming galaxy at $z \approx 5.5$ (Herrera-Camus et al. 2021). These authors found evidence for a [C II] emission extending beyond the dust and UV continuum disc, and forming a halo of ≈ 6 kpc in radius.

More recently, further signatures of [C II] haloes have been found at high redshift ($z \sim 7$), both in stacked and individual studies. Within the context of the REBELS survey (Bouwens et al. 2022), Fudamoto et al. (2022) observed a stacked [C II] emission $\times \sim 2$ larger than the dust continuum and the rest-frame UV ones, in agreement with the results of F20 at $z \sim 5$. This suggests that normal, star-forming galaxies present an extended [C II] emission feature over a wide range of redshifts. Using individual observations of the galaxy A1689-zD1 ($z = 7.13$), Akins et al. (2022) comes to the same conclusion by proving that the [C II] line is extended up to a radius $r \sim 12$ kpc, with the [O III] line and the UV-continuum not extending farther than $r \sim 4$ kpc.

The mounting observational evidence for the existence of these extended haloes inevitably calls for a thorough theoretical investigation of their origin, properties and evolution. In principle, these issues could be clarified by zoom-in cosmological simulations. With their ability to resolve structures down to molecular cloud scales, they are well suited to study the internal structure of primordial galaxies and of their circumgalactic medium (CGM; e.g. Pallottini et al. 2019). However – as shown by Fujimoto et al. (2019) – mock observations generated by using $z = 6$ zoom simulations (Pallottini et al. 2017b; Arata et al. 2019) fail to reproduce the observed [C II] surface brightness distribution of the emitting material in extended haloes. These independent studies agree in predicting a [C II] emission that is slightly more extended than the stellar continuum but drops very rapidly at distances considerably smaller than 10 kpc. The resulting profiles are characterized by a value of the

surface brightness which, in the external regions, is at least one order of magnitude lower than observed. This mismatch between theory and observations could originate either from issues in modelling FIR emission lines or because of some key physical ingredients that are not well captured by the numerical implementations adopted in the cosmological simulations. In any case, such tension represents a serious challenge in our understanding of early galaxy formation.

In order to bridge the gap between simulations and observational data, exploratory work can be useful to examine the physical implications of the observed emission, and guide the development of new simulations on the right track. In this context, Pizzati et al. (2020, hereafter P20) showed that the [C II] haloes observed by Fujimoto et al. (2019) can be reproduced by assuming that they are created by past (or ongoing) galactic outflow activity. In P20, we developed semi-analytical model for a supernova-driven galactic wind, and computed the [C II] emission expected to arise from the outflowing gas. We found very good agreement between the stacked Fujimoto et al. (2019) data and the model predictions, provided that (a) the outflow mass loading factor $\eta = \dot{M}/\text{SFR}$, where \dot{M} is the outflow rate, is relatively high ($\eta \approx 3$); (b) the escape fraction of ionizing photons from the parent galaxy is low ($f_{\text{esc}} < 1$ per cent). The first condition ensures that the density of the outflowing gas is high enough to match the observed [C II] surface brightness; the second prevents the galaxy radiation from ionizing the gas in the halo and leaving only scarce amounts of C II in the gas. For simplicity, we explored the two extreme cases $f_{\text{esc}} = 20$ per cent (i.e. photons from the galaxy dominate the radiation budget) and $f_{\text{esc}} = 0$ (i.e. the UV background is the dominant source of radiation in the halo), and find that only the latter scenario can explain the presence of the observed [C II] extended emission.

Here, we elaborate further on the possible connection between outflow activity and [C II] haloes by significantly improving the P20 model. In particular, we introduce a more realistic treatment of the gravitational influence exerted by the parent galaxy and its dark matter (DM) halo on the outflowing gas, and we account for the cosmic microwave background (CMB) suppression of the [C II] line (e.g. Vallini et al. 2015). We then compare the results of this updated model with the [C II] surface brightness profiles observed by the ALPINE survey (F20). We aim to study galaxies at the individual level, in order to characterize the properties of these systems and statistically infer possible scaling relations present at high redshift.

The paper is structured as follows. In Section 2, we summarize the main features of the P20 model, with particular emphasis on the improvements introduced in this work. Section 3 contains a brief overview of the ALPINE observational data used in this work. Sections 4 and 5 focus on the comparison between model results and ALPINE data. These results are discussed and interpreted in the framework of current galaxy formation and evolution theories in Section 6. Conclusions are given in Section 7.

2 OUTFLOW MODEL

The P20 model makes quantitative predictions on the properties of a [C II] halo generated by outflowing gas from a galaxy. It takes as inputs three key parameters: the outflow mass loading factor (η), the parent galaxy SFR, and circular velocity of the hosting DM halo (v_c). Once these three parameters are set, the model can predict the spatial distribution of the [C II] surface brightness produced by the outflowing gas. The profile can then be convolved with the same beam as the observations, and compared directly with data.

The model builds on previous studies of galactic winds: we consider the same setting as the pioneer work of Chevalier & Clegg

(1985, hereafter CC85). The active star forming region of the galaxy is modelled as a sphere of radius $R = 300$ pc. Energy and mass are uniformly injected from this region at a constant rate to mimic the input of supernovae (SN) associated with the star formation activity. This energy and mass deposition drives a spherically symmetric, hot, and steady wind that expands freely in the region outside the galaxy (the presence of the IGM/CGM is neglected).

As shown by e.g. Thompson et al. (2016), the assumption of adiabatic expansion in the original CC85 model breaks down for high values of the outflow mass loading factor ($\eta \gtrsim 1$). For large η values, then, the inclusion of radiative cooling results in a rapid decrease of the gas temperature, creating a cold/warm wind mode ($T \approx 10^{2-4}$ K) that propagates outward with lower velocity and higher density. This physical process is so abrupt and dramatic that it is known as *catastrophic cooling*, and it has been advocated by both semi-analytical models and simulations as one of the main cold wind formation channels (McCourt et al. 2018; Sarkar, Nath & Sharma 2015; Thompson et al. 2016; Scannapieco 2017; Schneider, Robertson & Thompson 2018; Gronke & Oh 2020; Fielding & Bryan 2022). In P20, we focus on this cooling scenario, as the formation and survival of [C II] in the gas is guaranteed only for relatively low temperature values ($T \lesssim 10^4$ K). Radiative losses are described in our wind equations by the net (i.e. cooling-heating) cooling function Λ , computed from the tables in Gnedin & Hollon (2012). We assume here solar metallicity for the gas, in accordance with the results of simulations at $z \approx 6$ (Pallottini et al. 2017a, 2022) and with the extrapolation of the mass–metallicity relation at high redshifts (Mannucci, Salvaterra & Campisi 2011, we are interested in the mass range of 10^9 – $10^{11} M_\odot$).

Under the hypothesis of photoionization equilibrium (PIE), the cooling (and heating) rates are strongly dependent on the ionizing radiation fields impinging on the gas. In turn, these fields can be produced either by leakage of ionizing photons from the parent galaxy, or by the cosmological contribution from all the other galaxies and quasars (the UV background, UVB). In P20, we extensively discuss how the overall properties of the wind depend on the relative intensity of these two radiation fields. As already explained in the Introduction, models in which f_{esc} is substantial, dramatically reduce the abundance of the C II ion by populating higher ionization states of the atom (C III, C IV). Thus, we follow P20 and fix $f_{\text{esc}} = 0$, i.e. we consider only we consider the UVB as the only radiation field acting on the gas.

Along with cooling, it is important to consider the gravitational effects of the galaxy disc and DM halo on the gas, which are neglected in the original CC85 formulation. This is an important effect: as the gas cools down radiatively, it slows down considerably, and thus its velocity becomes comparable with the escape velocity from the galactic system. In P20, the effects of the DM halo gravitational potential on the gas are included by parametrizing them with the halo circular velocity v_c .

With these assumptions, a cool wind that drives carbon (and other metals) into the CGM of the galaxy is produced. The wind is slowed down by the gravitational potential, and reaches a stalling radius r_{stop} at distances comparable with the sizes of the observed [C II] halo (Fujimoto et al. 2019). The hypothesis of PIE is then used to compute the abundance of neutral hydrogen and C II in the gas.¹ Together with the outflow temperature and density, relative abundances of H I and C II determine the emissivity of the [C II] line. Considering that the line is typically optically thin, a straightforward line integration

holds the [C II] surface brightness distribution. Further details about the outflow model and [C II] line emission predictions can be found in Sections 4 and 5 of P20, respectively. We now proceed on to detail two new specific improvements we have implemented with respect to P20.

2.1 Gravitational potential

Gravity can significantly slow down the gas expansion. This effect can be accounted for by introducing a gravitational potential $\phi(r)$ produced by a matter density distribution $\rho(r)$. Under the assumption of spherical symmetry, we can write the radial gradient of the potential as

$$\frac{d\phi(r)}{dr} = \frac{GM(r)}{r^2} = \frac{v_c^2(r)}{r}. \quad (1)$$

In this expression, M is the total mass contained in a sphere of radius r , and $v_c(r)$ is the local circular velocity:

$$v_c(r) = \sqrt{\frac{GM(r)}{r}} \quad (2)$$

The total mass is the sum of the DM halo contribution, $M_{\text{DM}}(r)$, and of the central galaxy’s baryonic component, $M_b(r)$.² In P20, we included only the contribution from the DM halo (neglecting the presence of the galactic disc) by assuming a singular isothermal sphere, for which $\rho \propto r^{-2}$. Such choice is particularly convenient because it yields $M \propto r$ and $v_c(r) = \text{const}$. Assuming an isothermal profile was a reasonable approximation in P20, as our aim was to compare our model only with stacked ALMA observations (Fujimoto et al. 2019). In this work, however, it becomes essential to model the effects of gravity in a realistic way to ensure a fair comparison between our model predictions and the individual galactic properties inferred from observations.

For this reason, we assume here a Navarro–Frenk–White (NFW; Navarro, Frenk & White 1997) density profile for DM. Hence, the DM total mass $M_{\text{DM}}(r)$ can be obtained analytically by integrating the density profile $\rho_{\text{NFW}}(r)$ in a volume of radius r :

$$M_{\text{DM}}(r) = \frac{M_{\text{vir}}}{\log(1+c) - \frac{c}{1+c}} \left[\log\left(\frac{r_s+r}{r_s}\right) + \frac{r_s}{r_s+r} - 1 \right], \quad (3)$$

where M_{vir} (r_{vir}) is the virial mass (radius) of the halo, c is the concentration parameter, and $r_s = r_{\text{vir}}/c$. Clearly, this is valid only for $r < r_{\text{vir}}$, which is canonically defined as $r_{\text{vir}} = (3M_{\text{vir}}/4\pi\delta_c\bar{\rho})^{1/3}$, where $\delta_c = 200$ is the mean halo overdensity with respect to the cosmic background density $\bar{\rho}$ at redshift z . For the concentration parameter, $c(M_{\text{vir}}, z)$, we adopt the fit given by Dutton & Maccio (2014).

We also include the baryonic contribution to the total mass. Consistently, with our assumption of spherical symmetry for the system, we adopt a Sersic profile with $n = 1$ (i.e. an exponential distribution) for the radial component of the stellar density:

$$\rho_b(r) = \frac{M_*(M_{\text{vir}}, z)}{8\pi r_*^3} e^{-r/r_*(r_{\text{vir}})}, \quad (4)$$

where M_* is the total stellar mass and r_* is the scale radius of the distribution. We link the halo mass M_{vir} and the stellar mass M_* – for a given redshift z – via the abundance matching approach of Behroozi, Wechsler & Conroy (2013). Further, we compute the radius r_* a function of the virial radius by introducing the spin parameter $\lambda = r_*/r_{\text{vir}}$, which we set to $\lambda = 0.01$ (Shibuya et al. 2015). By integrating

¹We use a carbon abundance $A_C = 2.69 \times 10^{-4}$ (Asplund et al. 2009).

²We neglect outflow self-gravity.

the density $\rho_b(r)$, we can then find the baryonic mass inside a sphere of radius r , $M_b(r)$, and consequently the total mass distribution $M(r)$ and the circular velocity $v_c(r)$. Note that in this formulation we are not accounting for the contribution of gas to the baryonic mass. This component may be a significant fraction of the total baryonic mass (e.g. Dessauges-Zavadsky et al. 2020); however, it is largely unconstrained and to a first approximation we neglect its presence in the galaxy mass budget.

The only parameters in this formulation are then the virial mass M_{vir} and the redshift z . Once they are set, we can characterize completely the halo gravitational potential $\phi(r)$ and study its effect on the outflow. In P20, we used the (constant) circular velocity v_c as a model parameter. Thus, here it is convenient to introduce a similar reparametrization of M_{vir} by defining the (dark-matter-only) circular velocity at the virial radius:

$$V_c \equiv \sqrt{\frac{GM_{\text{vir}}}{r_{\text{vir}}}}. \quad (5)$$

In the left-hand panel of Fig. 1, we plot $v_c(r)$ as a function of the galactocentric radius r , and for different values of the virial mass M_{vir} . Values of $v_c(r)$ are shown only for $r < r_{\text{vir}}$, where our region of interest resides. The dark-matter-only, isothermal-sphere case adopted in P20 is plotted for comparison with dashed horizontal lines. These lines also represent the value of the circular velocity at virial radius $V_c(M_{\text{vir}}, z)$. Fig. 1 (right-hand panel) quantifies the impact of different density profiles on the outflow velocity, v . Again, solid lines refer to the model used in this work, while dashed lines show the results for the P20 model. In these runs, the following fiducial values of the model parameters have been fixed: $\text{SFR} = 50 M_{\odot} \text{ yr}^{-1}$, $V_c = 200 \text{ km s}^{-1}$, and $z = 5$. The mass loading factor η is varied in the range $\eta \approx 0.5\text{--}7$. As detailed in P20, higher values of η result in lower launching velocities for the wind, and ultimately in lower stalling radii.

Adopting the NFW halo density profile considerably reduces the effects of gravity, especially for high values of η . Introducing the effects of baryonic matter increases the circular velocity in the central regions of the galactic system, but it does not have a strong impact on the evolution of gas at large radii ($r \gtrsim 5 \text{ kpc}$). As a result, the peak outflow velocity in the present is very similar to the one in P20, but the subsequent decrease is less steep here. Thus, the stalling radius r_{stop} is larger for a fixed value of the mass loading factor η .

2.2 CMB line suppression

Several works have pointed out that, as redshift progressively increases, CMB photons start to play an important role in regulating the FIR lines emission (Gong et al. 2012; da Cunha et al. 2013; Pallottini et al. 2015; Vallini et al. 2015; Kohandel et al. 2019). In particular, at $z \approx 4\text{--}6$, the temperature of CMB photons becomes high enough to produce an important effect on the overall [C II] emission of the gas. This effect is twofold: on the one hand, the CMB radiation field affects the atomic level populations, and hence the [C II] transition rate; on the other hand, the [C II] emission is observed against the CMB uniform background, which must be subtracted out when computing the [C II] surface density.

In P20, we ignored these effects for simplicity. However, as shown by e.g. Kohandel et al. (2019), their role in suppressing [C II] line emission in the external, low-density regions of high- z may be non-negligible. Thus, we take these effects into account by introducing the ratio ζ between the specific intensity of the [C II] emission observed against the CMB and the intrinsic one (see e.g. da Cunha et al. 2013).

This ratio can be written as (Gong et al. 2012):

$$\zeta = 1 - \frac{B_{\nu_*}(T_{\text{CMB}}(z))}{B_{\nu_*}(T_{\text{exc}})}, \quad (6)$$

where B_{ν} is the black body intensity and $\nu_* \simeq 1901 \text{ GHz}$ is the rest-frame frequency of the [C II] transition. The excitation temperature T_{exc} describes the effect of the CMB photons on the populations of the levels involved in the [C II] transition (i.e. the C II fine structure doublet, $^2P_{3/2} - ^2P_{1/2}$). An expression for T_{exc} is obtained in Appendix A (equation A6).

In Fig. 2 (left-hand panel), we show how the excitation temperature depends on two key parameters: the gas (electronic) density n_e , and the flux in the UV band – in the range $-19 < \log_{10}(I_{\text{UV}}[\text{ergs}^{-1}\text{cm}^{-2}\text{Hz}^{-1}\text{sr}^{-1}]) < -11$. Specifically, we show the ratio between the excitation temperature and the CMB one, $T_{\text{exc}}/T_{\text{CMB}}(z = 5)$. As such ratio approaches unity, the [C II] emission becomes indistinguishable from the CMB background, and thus the final [C II] flux is strongly suppressed.

We can identify three different physical regimes determining T_{exc} . For $n_e \gg 1 \text{ cm}^{-3}$, collisions dominate and the excitation temperature approaches the gas kinetic temperature T ; if a strong UV flux is illuminating the gas, the excitation temperature gets approximately equal to the UV colour temperature ($T_{\text{UV}} \approx 10^4 \text{ K}$; see equation A4); for low n_e densities and weak UV fluxes, instead, CMB photons dominate the transition rates, and thus the excitation temperature approaches T_{CMB} .

In order to account for CMB effects on [C II] emission in our model, we insert the suppression factor ζ (equation 6) in the integral defining the [C II] surface density. Exploiting the assumed spherical symmetry, we express $\Sigma_{\text{C II}}$ as a function of a single variable, the impact parameter b (i.e. the distance between the line of sight and the centre of the galaxy), by integrating the [C II] emissivity $\dot{\epsilon}_{\text{C II}} = n^2 \Lambda_{\text{C II}}$ (equation 17 in P20) along the line of sight:

$$\Sigma_{\text{C II}}(b) = \int_{-\infty}^{+\infty} \dot{\epsilon}_{\text{C II}} \zeta ds = 2 \int_b^{+\infty} \dot{\epsilon}_{\text{C II}}(r) \zeta(r) \frac{r}{\sqrt{r^2 - b^2}} dr. \quad (7)$$

This integral depends implicitly on the thermodynamic and ionization state of the outflow, as well as the ionizing radiation field contributions from the galaxy and the UVB.

As an illustration, in Fig. 2 we show the b dependence of the surface brightness profiles as a function of the mass loading factor η . The other parameters are set to their fiducial values (see Section 2.1). From the figure, we see that the suppression of the [C II] emission can be significant. The effects are dramatic for low η values ($\zeta \approx 0.05\text{--}0.3$), and more moderate (but still relevant) in the high η range ($\zeta \approx 0.3\text{--}0.8$). Therefore, we conclude that CMB suppression plays an important role in regulating the total [C II] emission at high redshift, by diminishing the total [C II] luminosity and favouring high gas densities in the outflow (or, equivalently, high values of the mass loading factor). The surface density profiles shown in Fig. 2 are converted into fluxes per unit area (see equation 24 in P20) and convolved with the same beams as the observations by F20. These final steps allow us to directly compare the model results to the observations.

3 ALPINE SAMPLE

The ALMA ALPINE survey (Le Fèvre et al. 2020; Faisst et al. 2020; Béthermin et al. 2020) targeted 118 normal, star-forming ($10 \lesssim \text{SFR}/M_{\odot} \text{ yr}^{-1} \lesssim 100$) galaxies at $z \approx 4\text{--}6$. It measured the spatial distribution of the [C II] line (64 per cent detection rate) and the (rest-frame) FIR continuum (21 per cent). On top of that, it exploited

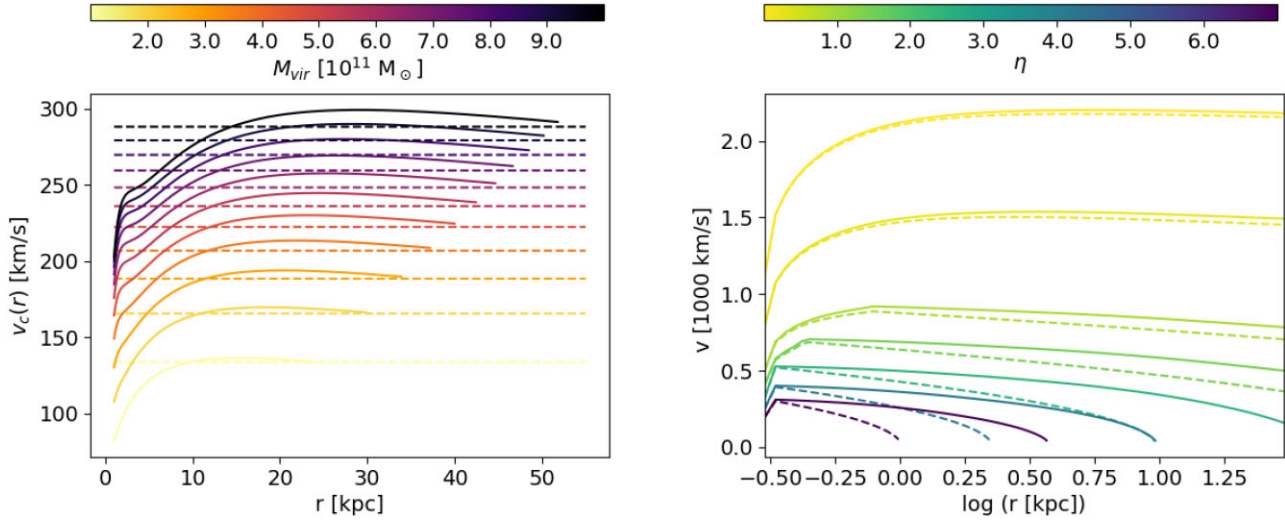


Figure 1. *Left:* Circular velocity, v_c , as a function of radius for a NFW halo density profile (Navarro et al. 1997) and a Sersic-like stellar distribution (solid lines). Different haloes are colour-coded according to their virial mass, M_{vir} . The dashed lines represent the profiles for v_c employed in P20, and also the values of V_c that are used as parameters in our model. *Right:* Outflow velocity (note the different scale with respect to the left-hand panel) for different values of the mass loading factor η . The other parameters are fixed to the fiducial values reported in the text. The NFW + bulge (isothermal sphere) case is shown with solid (dashed) lines.

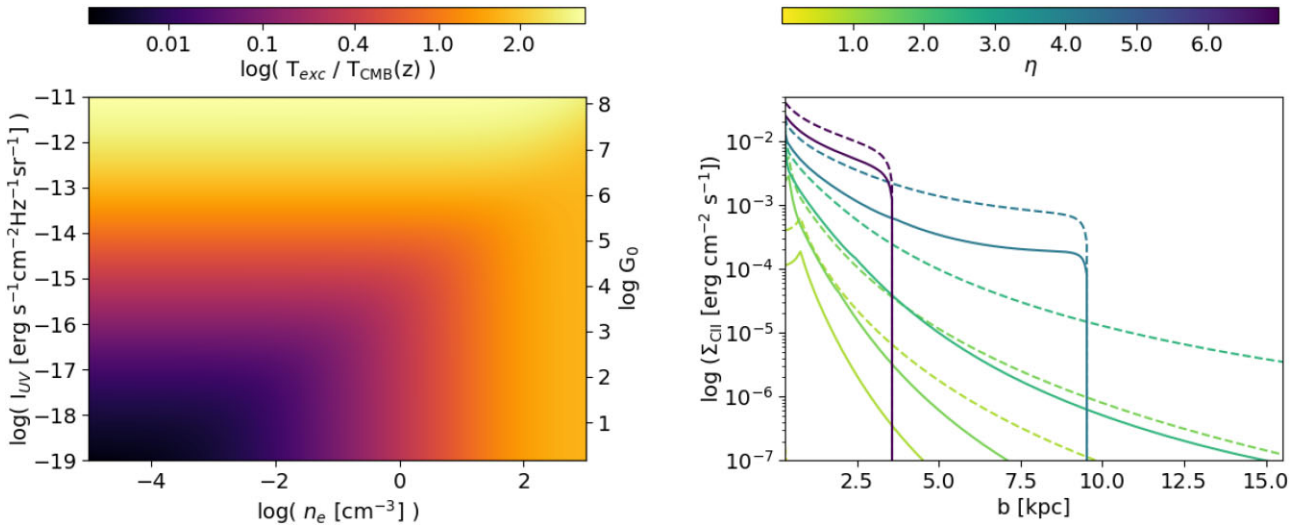


Figure 2. *Left:* Heat map showing the ratio between the excitation temperature and the CMB one ($T_{\text{exc}}/T_{\text{CMB}}(z)$), computed at redshift $z = 5$, as a function of the free electron density, n_e , and UV radiation field intensity, I_{UV} at 1330 Å. The latter quantity is also expressed in terms of the Habing flux G_0 (in units of the averaged Milky Way value $1.6 \times 10^{-3} \text{ erg cm}^{-2} \text{ s}^{-1}$; right axis). The gas temperature is assumed to be $T = 10^3 \text{ K}$, and the gas electron fraction is fixed to $x_e = n_e/n = 0.5$. *Right:* [C II] surface density Σ_{CII} (equation 7) as a function of the impact parameter b , for different values of the mass loading factor η . Solid (dashed) lines show the results with (without) the inclusion of CMB suppression.

observations from *HST*, *VLT*, and *Spitzer* to build a multiwavelength catalogue for these systems (Faisst et al. 2020).

F20 analyse ALPINE observations focusing on the extension of the [C II] emitting galactic haloes. They select the 23 galaxies from the ALPINE sample whose [C II] emission is observed above the 5σ level, and they compare the (averaged) radial profile of the [C II] line with the ones of the rest-frame UV (stellar) and FIR (dust) continuum.

Out of these 23 galaxies, they identify 7 systems belonging to the ‘[C II] halo’ category. These are defined as systems whose peripheral region (i.e. the region obtained by masking the central galaxy contribution) shows a [C II] line at $>4\sigma$ and the (rest-frame) UV and FIR continuum at $<3\sigma$. Note that such thresholds inevitably

depend on the sensitivity of observations. New, deeper observations could in principle reveal the presence of [C II] haloes even in other ALPINE systems that were not inserted in the ‘[C II] halo’ category by F20 (for more details, see Herrera-Camus et al. 2021). However, this classification is the first attempt to characterize [C II] haloes in individual high- z galaxies and to study the statistical properties of their host systems. For this reason, the work of F20 is ideally suited for comparing the outputs of our model with observational data.

The 7 ‘[C II] halo’ galaxies identified in F20 have redshifts in the range $z_{\text{CII}} \approx 4.5\text{--}5.5$, $\text{SFR} > 15 M_{\odot} \text{ yr}^{-1}$, and stellar masses $M_* > 5 \times 10^9 M_{\odot}$. In Table 1, we report the value of z_{CII} , SFR, and M_* inferred from observations. Redshifts are measured spectroscopically

Table 1. Properties of the ‘C II halo’ sample taken from the F20 study. From left to right: name of the ALPINE source (‘DC’ stands for ‘DEIMOS COSMOS’, while ‘VC’ stands for ‘VUDS COSMOS’); values of redshift ($z_{\text{C II}}$), SFR, and stellar mass (M_*) taken from Faisst et al. (2020); halo mass (M_{vir}) and global circular velocity (v_c) inferred from Behroozi et al. (2013); results from our MCMC analysis, i.e. median and 1σ uncertainties of the posterior distributions for the three parameters considered in our model: η , SFR, and V_c ; χ^2 of the model-data comparison for the values of the parameters that maximize the posterior distribution, Θ_{max} . Uncertainties on the redshift measurements are very small and not shown here.

ID	$z_{\text{C II}}$	Galaxy data				Model Predictions			$\chi^2(\Theta_{\text{max}})$
		SFR ($M_\odot \text{ yr}^{-1}$)	M_* ($10^9 M_\odot$)	M_{vir} ($10^{11} M_\odot$)	V_c (km s^{-1})	SFR ($M_\odot \text{ yr}^{-1}$)	V_c (km s^{-1})	η	
DC396844	4.54	55^{+40}_{-25}	$7.3^{+2.6}_{-2.6}$	$4.4^{+2.8}_{-1.8}$	210^{+90}_{-66}	64^{+51}_{-29}	170^{+54}_{-46}	$5.1^{+2.2}_{-1.6}$	3.6
DC630594	4.44	31^{+24}_{-15}	$5.9^{+2.3}_{-1.7}$	$3.9^{+2.6}_{-1.5}$	199^{+85}_{-59}	34^{+32}_{-16}	196^{+43}_{-47}	$6.8^{+4.6}_{-2.4}$	4.1
DC683613	5.54	58^{+44}_{-26}	$14.7^{+5.7}_{-4.4}$	$6.7^{+5.9}_{-3.7}$	241^{+145}_{-102}	84^{+60}_{-44}	160^{+72}_{-44}	$4.8^{+2.0}_{-1.5}$	2.7
DC880016	4.54	32^{+25}_{-15}	$5.6^{+2.3}_{-1.6}$	$3.7^{+2.6}_{-1.4}$	197^{+85}_{-58}	37^{+30}_{-17}	170^{+51}_{-40}	$5.5^{+2.5}_{-1.8}$	5.8
DC881725	4.58	88^{+61}_{-43}	$9.1^{+4.0}_{-2.1}$	$4.9^{+3.5}_{-2.1}$	217^{+98}_{-68}	102^{+50}_{-44}	222^{+75}_{-82}	$4.3^{+3.2}_{-1.2}$	4.1
VC5100537582	4.55	15^{+14}_{-6}	$5.7^{+2.0}_{-1.6}$	$3.8^{+2.6}_{-1.4}$	198^{+83}_{-58}	23^{+15}_{-9}	162^{+29}_{-27}	$6.9^{+2.7}_{-2.0}$	9.5
VC5110377875	4.55	99^{+79}_{-41}	$14.7^{+4.7}_{-5.6}$	$6.8^{+5.1}_{-3.9}$	243^{+125}_{-97}	107^{+78}_{-49}	241^{+63}_{-41}	$3.7^{+2.0}_{-1.1}$	4.4

using the [C II] line, while SFRs and stellar masses are inferred from SED fitting of the multiwavelength ancillary data (Faisst et al. 2020).

As detailed in Section 2.1, we convert the values of the stellar masses inferred observationally into DM halo virial masses using the fitting functions obtained by Behroozi et al. (2013). We also compute the resulting circular velocity at virial radius from equation (5). We obtain virial masses in the range $M_{\text{vir}} \approx (3-7) \times 10^{11} M_\odot$ and circular velocities $V_c \approx 200-250 \text{ km s}^{-1}$. For reference, these quantities are shown in Table 1 together with the rest of observational data.

4 COMPARISON WITH DATA

We now proceed to compare our model predictions with the observed [C II] profiles for the seven systems presented in Section 3. We take as parameters in our model the mass loading factor ($\log \eta$), the \log SFR, and the circular velocity ($\log V_c$). For every one of the systems considered, we assume flat priors on $\log \eta$, and use the information presented in Section 3 to set Gaussian priors on \log SFR and $\log V_c$ (the median and variance are chosen according to the values reported on Table 1). A detailed discussion of our methods is given in Appendix B.

We run a Markov chain Monte Carlo (MCMC) using the PYTHON package EMCEE to explore the posterior distributions. As an illustration, the corner plot in Fig. 3 shows the 1D and 2D marginalized posterior for one of the galaxies in the sample, DC396844. The same plots for the other galaxies are shown in Appendix C (Fig. C1). The predicted median values and 1σ errors of the different parameters are given on the right side of Table 1.

We also show the values of $\chi^2(\Theta_{\text{max}})$ (computed at the peak of the posterior distribution, Θ_{max}) in the last column of Table 1. We find that the χ^2 are reasonably low (the number of degrees of freedom for our three-parameter model is $\text{ndof} = 6$), implying that our model reproduces observations quite well. This can be confirmed visually by the right-hand panel of Fig. 3, where we plot the observational data (red points) along with synthesized emission profiles from our model (grey lines), created by randomly sampling the posterior distribution.

5 RESULTS

The corner plots shown in Figs 3 and C1 reveal that, for most sources, there is evidence for a bimodal shape of the posterior distribution. The origin of the bimodality can be understood focusing on the emission profiles for DC396844 (the right-hand panel of Fig. 3): the

[C II] profiles for low- V_c haloes are even more extended than the observed ones; on the contrary, higher V_c values result in a more compact emission that is barely compatible with the observed ones. Given the large relative uncertainty on data points at large impact parameter, both behaviours are consistent with the data.

In almost all cases, the recovered values for SFR and V_c (blue-shaded regions in the corner plots) match very well the independent determinations from the SED fitting (red-shaded regions). This is partly due to our choice for the prior distributions; even so, given the good agreement between our model and the data profiles, it signifies that well-matching solutions can be found for values of the SFRs and stellar masses that are compatible with observational estimates.

The posterior distributions we obtain for the η parameter are particularly interesting, as they represent one of the few (indirect) measurements of the mass loading factor available at the high redshift. As shown in Table 1, we infer relatively high median values for the mass loading factor, $4.3 \leq \eta \leq 6.8$.

As the mass loading factor depend on the SFR and stellar mass of galaxies, it is useful to plot the predicted values of η as a function of these two physical properties. In Fig. 4, we plot the results and perform power-law fits, finding that both $\eta - M_*$ and $\eta - \text{SFR}$ are inversely correlated. The best-fitting power-law scalings are as follows:

$$\log \eta = (-0.43 \pm 0.14) \log(M_*/10^{10} M_\odot) + \log(4.7 \pm 0.3), \quad (8)$$

$$\log \eta = (-0.32 \pm 0.05) \log(\text{SFR}/M_\odot \text{ yr}^{-1}) + \log(17.5 \pm 3.6). \quad (9)$$

The dependence $\eta \propto M_*^{-0.43}$ is close to that expected from a momentum-driven outflow, for which $\eta \propto M_*^{-1/3}$ (Finlator & Dave 2008; Davé, Finlator & Oppenheimer 2012). This is consistent with the fact that outflowing gas in our model solutions loses much of its thermal energy via radiative cooling in a region very close to the launching site (Section 2). The analogue dependence for the $\eta - \text{SFR}$ is a consequence of the galaxy main sequence, where most of the ALPINE systems reside (Faisst et al. 2020).

Numerical simulations of starburst galaxies also find mass loading factors that are compatible with momentum-driven outflows. For instance, Muratov et al. (2015) uses the FIRE zoom cosmological simulations (Hopkins et al. 2014) to obtain the following power-law relation with stellar mass M_* :

$$\log \eta = (-0.36 \pm 0.02) \log(M_*/10^{10} M_\odot) + \log(3.6 \pm 0.7). \quad (10)$$

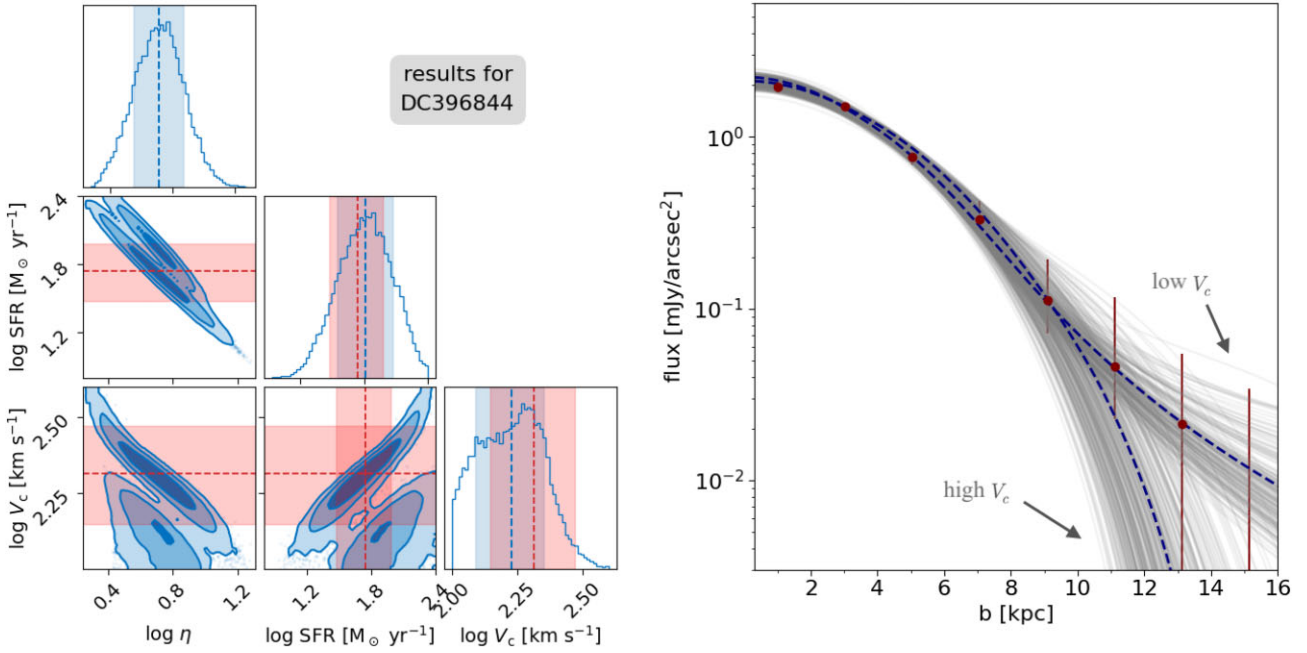


Figure 3. *Left:* Corner plots of the 3D posterior distribution $P(\log \eta, \log \text{SFR}, \log V_c | d, m)$ for the galaxy DC396844. The values of the parameters SFR and V_c inferred from observations (Table 1) are shown with red dashed lines, together with their uncertainties (red shaded regions). The blue dashed vertical lines represent the median values of the parameters (1σ errors are again shown as shaded regions). Similar plots for the full ALPINE ‘[C II] halo’ sample are shown in Fig. C1. *Right:* Comparison of predicted [C II] profiles (light grey lines) obtained for DC396844 with the observed one (F20, red points). The theoretical profiles are generated by randomly sampling the posterior distribution 500 times. The blue dashed lines correspond to the values of the parameters for which the posterior exhibits a local peak (see left-hand panel).

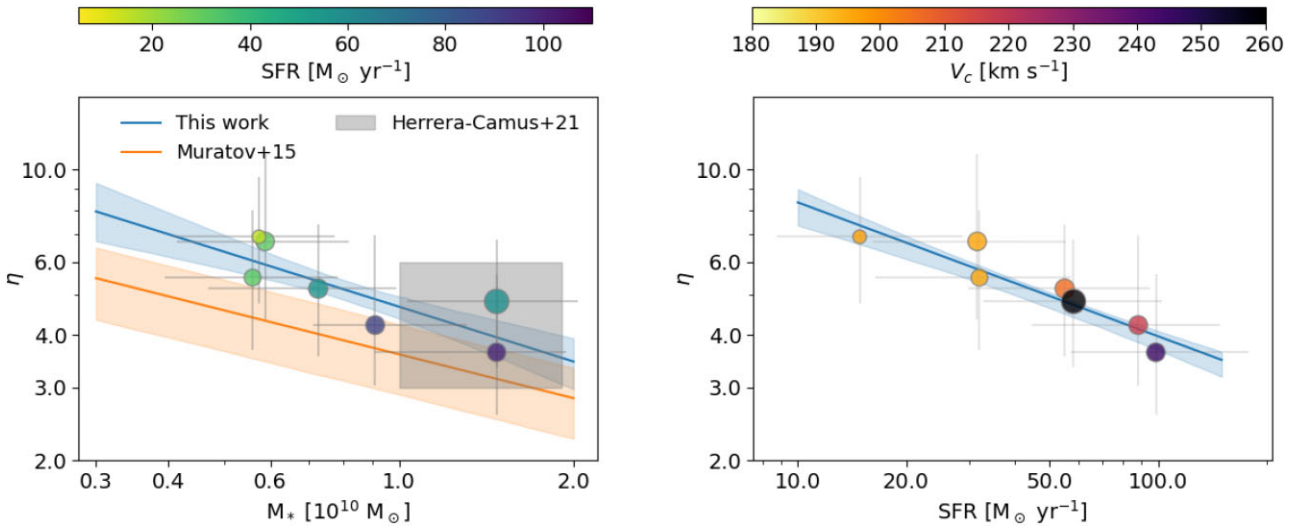


Figure 4. *Left:* Dependence of the mass loading factor η (shown are median values and associated 1σ error) on the stellar mass M_* . Stellar masses are obtained from observational data (Table 1). The blue line shows the best power-law fit to the data. For reference, we also show predictions from simulations (Muratov et al. 2015, orange, equation 10) and observations Herrera-Camus et al. (2021, grey rectangle). Data points are colour-coded according to their SFR, as inferred from observations. The size of every point is proportional to the value of the likelihood $\mathcal{L}(\Theta_{\max})$ (equation B1). *Right:* Same as left-hand panel, but for the SFR. The colour of the data points corresponds to their virial velocity V_c (see colourbar), as described in Table 1.

We add this relation to our results in Fig. 4 for comparison. We find a perfectly compatible scaling, but our values of η tend to be systematically higher; it is hard, however, to tell whether this difference ($\approx 1 - 2\sigma$) is due to some systematical bias (see Section 6.2 for more details) or it contains some interesting physical insight.

Note that, in principle, the presence of additional energy sources such as active galactic nuclei (AGNs) may disrupt the simple power-law scaling between η and M_* (see e.g. Zhang et al. 2021). We do not expect, however, our sample to be affected by this, as galaxies in the ALPINE catalogue show no sign of AGN activity (Barchiesi et al. 2022; Faisst et al. 2022).

6 DISCUSSION

In this work, we have applied the (improved) P20 model to ALPINE systems showing signs of extended [C II] emission, arguing that (a) detected [C II] haloes are a natural by-product of starburst-driven outflows; (b) the mass loading factors of these outflows have values in the range $4 \lesssim \eta \lesssim 7$ and scaling compatible with the momentum-driven hypothesis. In the following, we further elaborate on this picture by investigating its consequences and comparing it with previous studies.

6.1 Halo-outflow connection: observational evidence

Given that the ubiquity of galactic winds at all redshifts and their key role in shaping galaxy properties have been widely acknowledged (Rupke 2018), a causal connection between outflows and the formation of [C II] haloes seems at least plausible. However, this connection needs to be backed up by direct observational evidence of galactic winds in [C II] halo-hosting systems. The best way to probe the presence of these winds is by studying the kinematics of the gas. Looking at the spectrum of the [C II] line, in fact, it is possible to search for a broad component that is commonly associated with the presence of outflowing gas. Indeed, several works have already found preliminary evidence for this. The first discovery of [C II] haloes in normal star-forming galaxies (Fujimoto et al. 2019) was accompanied by a statistical indication of the presence of broad wings in the stacked [C II] spectra of nine of these $z \approx 6$ galaxies (Gallerani et al. 2018). In the context of the ALPINE survey, Ginolfi et al. (2020) performed a stacking of the [C II] spectra of a subsample of ALPINE galaxies, finding evidence for a broad Gaussian feature (HWHM $\approx 275 \text{ km s}^{-1}$) that becomes even more prominent when only highly star-forming (SFR $> 25 M_{\odot} \text{ yr}^{-1}$) systems are considered.

An even more convincing sign of the direct link between haloes and outflow activity comes from deep observations of the individual system HZ4 (Herrera-Camus et al. 2021). In addition to the spatially extended [C II] emission already mentioned in Section 1, from the line broad wings the authors identify the presence of an outflow in two adjacent sub-regions of $\approx 2 \text{ kpc}$ size, extending from the central disc in the direction of the minor axis. These findings point to the presence of an active outflow, with velocities in the range $v \approx 300\text{--}400 \text{ km s}^{-1}$, launched from the inner galactic regions and reaching out the CGM, that is detected as [C II] extended emission.

The above body of evidence, although still limited in size and robustness, supports the outflow-halo model proposed in this work. Our model, in fact, is characterized by gas velocities ranging (for the best-fitting η values) from $v \approx 200 \text{ km s}^{-1}$ to $v \approx 500 \text{ km s}^{-1}$ (Fig. 1, right-hand panel). Such values of the gas velocity are comparable to the halo virial velocity, V_c (Fig. 1, left-hand panel). This implies that outflows are likely unable to escape the global gravitational potential of the galaxy. Rather, the expelled gas builds up a relatively high-density and high-metallicity halo that can survive for several dynamical timescales of the parent galaxy. Also, we predict that [C II] emission extends out to $r \approx 15 \text{ kpc}$, which is in very good agreement with observed halo sizes.

This general concordance between the wind model considered here and observational evidence for [C II] haloes does not rule out the possibility that alternative wind models are also compatible with the formation of haloes at the high redshift. For instance, cold wind modes (for which the amount of C II is expected to be significant, see P20 for more details) can also be formed by ISM clouds that are entrained in the hot outflowing medium. However, despite the fact

that many theoretical efforts have been directed to study the evolution of these clouds in the wind (e.g. Scannapieco & Brügger 2015; McCourt et al. 2015; Brügger & Scannapieco 2016; Schneider & Robertson 2017) – a general consensus on the role of this mechanism as a viable cold-mode formation channel has yet to be reached. As Fielding & Bryan (2022) suggests that it is possible that both radiative cooling of hot gas and cold-cloud entrainment can play a role in determining the final multiphase structure of the outflow. Further work is needed to investigate whether this scenario gives rise to an extended [C II] emission in agreement with observations.

Two additional remarks are worth adding here. First, the presence of a halo does not necessarily imply an ongoing outflow, i.e. some haloes maybe be remnants of past outflow activity and could be observed well after gas ejection from the galaxy has ended. This situation might, however, easily lead to the non-detections reported by F20 and Spilker et al. (2020) as the low velocities implied make the identification of the broad wings problematic. Secondly, we underline that our model describes a steady-state solution (for details, see P20), which implicitly requires that the outflow lasts for several [C II]-halo crossing times ($\approx 50 \text{ Myr}$). If the system is caught at early times, the outflow might not yet have had sufficient time to build the halo.

6.1.1 [C II] halo non-detections

If SF-driven outflows are responsible for the formation of [C II] haloes, then it is fair to ask why haloes are not observed in every starburst galaxy. In fact, one of the key findings of F20 is that not all of the galaxies are [C II] halo hosting systems. About ~ 25 per cent of them (~ 70 per cent considering galaxies classified as ‘other’) show no detectable signs of extended [C II] emission. Interestingly, these authors find that galaxies belonging to this ‘no [C II] halo’ class tend to have lower SFRs and stellar masses with respect to [C II] halo-hosting ones. A similar conclusion was also drawn by Ginolfi et al. (2020), whose stacking revealed the presence of extended [C II] emission only for the subsample of galaxies with SFR $> 25 M_{\odot} \text{ yr}^{-1}$.

A possible explanation for these trends is that low-mass and low-SFR galaxies cannot launch outflows that are powerful enough to transport carbon away from the galactic centre. However, such hypothesis is in contrast with the fact that outflows are seen in simulations in every mass range, and are expected theoretically from the metal enrichment scenario at high- z (e.g. Davé et al. 2012; Wise et al. 2014; Pallottini et al. 2014); even more critically, in low mass systems they might be more prominent as a result of their larger mass loading factors (see Section 5 and Muratov et al. 2015).

Our model naturally offers a different interpretation for the non-detections. In low-mass systems, outflows are indeed present and transport carbon into the circumgalactic medium, but the resulting extended emission is too faint to be detected with the current level of sensitivity. This can be showcased by considering our model with two different values of the stellar mass: $M_* = 10^9 M_{\odot}$ (labelled as *low mass*) and $M_* = 10^{10} M_{\odot}$ (*high mass*). Using the $\eta - M_*$ (equation 8) and $\eta - \text{SFR}$ (equation 9) relations, as well as the stellar mass-halo mass relation from Behroozi et al. (2013), we can express the three model parameters as a function of M_* only. In particular, $M_* = 10^9 M_{\odot}$ corresponds to $(\eta, \text{SFR}, V_c) = (12.8, 2.6 M_{\odot} \text{ yr}^{-1}, 143 \text{ km s}^{-1})$; for $M_* = 10^{10} M_{\odot}$, we find $(4.7, 62 M_{\odot} \text{ yr}^{-1}, 218 \text{ km s}^{-1})$.

In Fig. 5 (upper panel), we plot the surface brightness of the [C II] emission for these two runs. The high-mass system has a larger

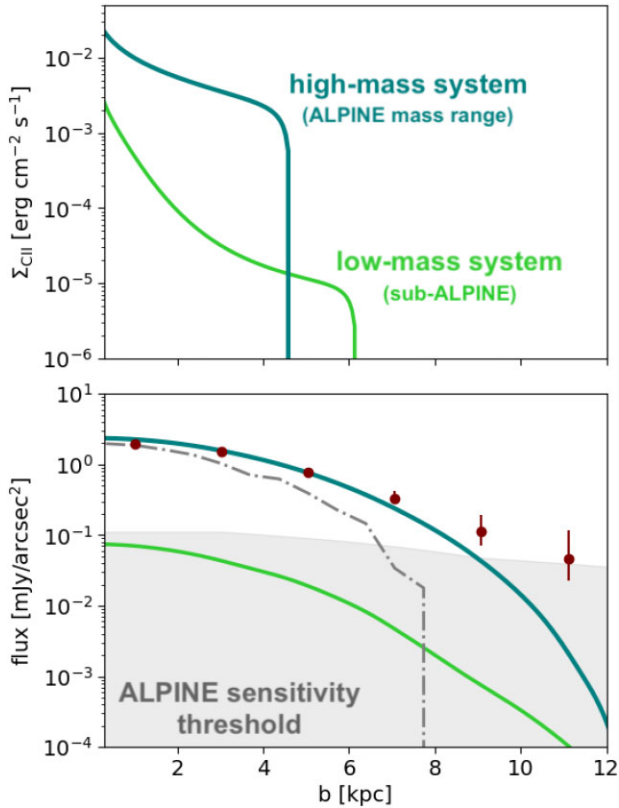


Figure 5. *Top:* [C II] surface density $\Sigma_{\text{C II}}$ (equation 7) as a function of the impact parameter b , for the two runs considered in Section 6.1.1. The low-mass system (green line) has a stellar mass of $M_* = 10^9 M_\odot$, corresponding to a mass loading factor $\eta = 12.8$, an SFR = $2.6 M_\odot \text{ yr}^{-1}$, and a circular velocity $V_c = 143 \text{ km s}^{-1}$. The high-mass system (teal line), instead, has $M_* = 10^{10} M_\odot$, $\eta = 4.7$, SFR = $62 M_\odot \text{ yr}^{-1}$, $V_c = 218 \text{ km s}^{-1}$. *Bottom:* Predicted flux for the two systems, obtained by convolving the surface brightness with the same beam as observations (dash-dotted grey line) and converting the units to mJy arcsec^{-2} . In this way, a direct comparison with observational data is possible (the data points correspond to the system DC396844 and are shown only as a reference). The grey-shaded region shows the ALMA sensitivity threshold for ALPINE observations.

surface brightness at all radii, but the profile is quite compact, because the outflow is halted by gravity at $\simeq 4.5 \text{ kpc}$ from the launching site. On the other hand, the low-mass one is more extended, but the absolute value of the surface brightness is $10\times$ lower at the centre, also showing a steeper radial decline.

Concluding that larger η values correspond to dimmer profiles may seem counterintuitive, as one might naively expect that an outflow with high η is loaded with more material. However, the relatively shallow $\eta(M_*)$ trend in momentum-driven winds implies that it is the SFR, rather than η , that ultimately governs the mass outflow rate for a system. More massive and star-forming systems are therefore characterized by mass-loaded outflows that can be dense and bright enough to form extended haloes in [C II].

This is clear by looking at the bottom panel of Fig. 5, where we convolve the surface brightness profiles with the ALMA beam and transform the surface brightness in a flux per unit solid angle (measured in mJy arcsec^{-2}). We have assumed the beam size, redshift, and FWHM of the system to be equal to those of DC396844; such choice does not affect our conclusions in any relevant way. As a reference, we also plot the data for DC396844 (red points), as well as the associated line sensitivity (grey-shaded region) taken from

F20 (corresponding to an integration time of $\sim 20 \text{ min}$, Béthermin et al. 2020). The flux of the high-mass system is well above the noise level, and reaches an effective size of $r \gtrsim 10 \text{ kpc}$, which is partly due to beam smoothing. Thus, this system would be classified as a galaxy with a [C II] halo. On the other hand, the low-mass system flux radial profile is very faint: it is slightly below the ALMA sensitivity level at the centre, and it declines rapidly such that the region extending farther than the beam size has a very low surface brightness ($\sim 10^{-3} \text{ mJy arcsec}^{-2}$).

These results are in line with observations, as a mass of $M_* = 10^{10} M_\odot$ falls exactly in the range where [C II] haloes have been detected by the ALPINE survey (Table 1). The low-mass system ($M_* = 10^9 M_\odot$) is instead representative of the group of low-mass/low-SFR galaxies whose [C II] emission is not extended enough to be classified as a halo by F20 and by the Ginolfi et al. (2020) stacking. Probing the presence of [C II] haloes in this set of galaxies with future observations may not be trivial, as a very high sensitivity is required due to the steep decrease in surface brightness at large radii. The optimal solution could consist in improving both the sensitivity level and the angular resolution of observations, in order to constrain the emission in the peripheral region at $r \sim 4\text{--}8 \text{ kpc}$.

The above discussion argues in favour of a picture in which starburst-driven outflows are widespread in high- z galaxies at all masses. The detection of the extended [C II] emission associated with this outflow activity, however, is subject to the sensitivity level and spatial resolution of observations. We highlight the fact that this discussion is useful to interpret the general trends observed in F20, but it is not able to capture the differences in the halo properties that the authors found in systems with very similar stellar masses and SFRs. We expect that other factors, such as time-dependent effects discussed above and not included in our simplified model, may contribute to create these differences.

6.1.2 The role of the escape fraction

Finally, we also point out that the arguments presented here are somewhat sensitive to the assumptions concerning the ionizing photon escape fraction, $f_{\text{esc}} \ll 1$ (see Section 2). A negligible escape fraction is a key requirement for our model to be compatible with the observed halo luminosities, as photons emitted from the central galaxies drastically reduce the amount of neutral gas in the outflow. However, the conclusion $f_{\text{esc}} \sim 0$ holds true only for galaxies that have been observed to host a [C II]. Indeed, since f_{esc} has a major impact on the formation of [C II] haloes, its variation in different mass ranges (e.g. Xu et al. 2016; Wise et al. 2014) could also be responsible for the absence of observed [C II] haloes in low-mass systems. If this is the case, then we foresee the opportunity of using the presence of [C II] haloes as a tracer of f_{esc} at high redshifts. The *JWST* could help us testing this by determining the value of the escape fraction in the low-mass, low-luminosity range (Chisholm et al. 2018).

A small but non-negligible value of f_{esc} is expected in low masses galaxy, which are the main driver of the first stages of Reionization (e.g. Ma et al. 2020). However, the presence of neutral gas in the CGM is not in contrast with the leakage of ionizing photons from the central galaxy, as photons preferentially escape through low-column density paths that cover only a small fraction of the solid angle (e.g. Stern et al. 2021). For this reason, we can speculate that high f_{esc} channels provide a sufficient amount of ionizing photons to reionize the IGM, while, at the same time, the thermal/ionization structure of the outflows is preserved in most of the volume. This possibility

can be explored within our model by dropping the assumption of spherical symmetry. We defer this study to future work.

6.2 Outflow mass loading factors

It is interesting to compare the mass loading factors we obtain in Section 5 ($4.3 < \eta < 6.8$) with observational estimates, both at low and high redshifts. However, it is important to highlight the fact that our analysis focuses only on the systems showing clear evidences of a [C II] halo. Therefore, the values of η we find are representative only of this special class of high- z galaxies, which may be a biased sub-sample of the whole high- z , star-forming galaxies population.

Moreover, although the outflow properties largely depend on η as shown by Thompson et al. (2016), other model parameters such as the wind energy coupling and the number of supernovae per unit stellar mass (α and ν in P20, respectively) may also play a role in determining the final extension and property of the resulting [C II] halo. In P20, we assumed $\alpha = 1$ (consistently with observational estimates from Strickland & Heckman 2009) and $\nu = 0.01 M_{\odot}^{-1}$. Although reasonable, different choices for these parameters may affect the optimal η range found in this work.

With these caveats in mind, we briefly review other estimates in the literature. A relevant work by Heckman et al. (2015) uses UV absorption lines to study the properties of starburst-driven outflows in local starburst galaxies. They find that η weakly anticorrelates with both SFR and V_c (or, equivalently, M_*), and $1 \lesssim \eta \lesssim 4$. This range is lower than the one we find in our study. This discrepancy may be explained by an evolution of η with redshift (e.g. Nelson et al. 2019), which is expected given the different properties of the ISM in high- z galaxies (Pallottini et al. 2022). Other estimates, however, find significantly larger η values, which are compatible with our conclusions. For instance, using H α emission lines originating in the CGM of local galaxies, Zhang et al. (2021) measure η in different ranges of halo masses. In the range relevant for the ALPINE galaxies studied here, they find $2 \lesssim \eta \lesssim 7$, in very good agreement with the values found here.

The Ginolfi et al. (2020) analysis of stacked ALPINE systems gives relatively low values of η (≈ 0.5 – 2). However, Herrera-Camus et al. (2021) – using deep observations of the galaxy HZ4 – find similar η values only when considering the *total* SFR of the galaxy. According to their study, only a sub-region of the galaxy is driving the wind; when computing the mass loading factor by using the local SFR of the regions showing signs of outflow activity, they find $\eta = 3$ – 6 (grey-shaded box in Fig. 4). This estimate is compatible with our results and suggests that measurements of the mass loading factors could be underestimated when considering the entire galaxy as the outflow launching site. Deeper observations are needed to determine whether this is the case for the majority of galaxies in the ALPINE sample.

7 SUMMARY

In this work, we showed that the recently discovered, extended (≈ 10 – 15 kpc) [C II] emitting haloes around high- z galaxies can be produced by ongoing (or past) outflow activity. We improved and extended the model presented in P20, by adopting a more realistic (DM + baryons) density distribution, and accounting for the effects of CMB suppression. Our model generates synthetic [C II] radial profiles depending on three key parameters: the outflow mass loading factor (η), the galaxy SFR, and the parent DM halo circular velocity at virial radius (V_c). Using a MCMC-based approach, we compare our

model with individual targets in the ALPINE survey (Fujimoto et al. 2020), and infer the values of these parameters for each [C II] halo-hosting system. The results are summarized as follows:

(i) Our improved model is in broad agreement with the results from P20: outflows launched by SN explosions in the centre of galaxies expand in CGM with velocities in the range of 200 – 500 km s $^{-1}$. Within the first kpc, the gas catastrophically cools to $T \approx \text{few} \times 100$ K, and then it is slowly heated up again to $T \approx 10^3$ K by the cosmic UV background. Such conditions are favourable for the formation of C II ions. If the escape fraction of ionizing photons from the parent galaxy is low ($\lesssim 1$ per cent), the outflows remain largely neutral, with a significant C II abundance at any stage of their evolution.

(ii) The halo gravitational pull slows down the outflow, typically stopping it completely at $r \approx 10$ – 15 kpc. These values are perfectly compatible with the extension of the observed [C II] emission. Gravitational effects are particularly important for large η values.

(iii) CMB can suppress the [C II] emission of the halo by a factor of 2 – 4 . Even accounting for this suppression the observed [C II] luminosity ($L_{\text{C II}} \approx 5$ – $15 \times 10^8 L_{\odot}$) can be recovered.

(iv) By comparing our model predictions with observational data of individual galaxies in the ALMA ALPINE survey, we show that (a) detected [C II] haloes are a natural by-product of starburst-driven outflows; (b) the mass loading factors of these outflows have values in the range $4 \lesssim \eta \lesssim 7$ and scalings compatible with the momentum-driven hypothesis ($\eta \propto M_*^{-0.43}$).

(v) Our model (and simulations in the literature) suggest that outflows are widespread phenomena in high- z galaxies. However, in low-mass systems the halo extended [C II] emission is likely too faint to be detected with the current sensitivity levels.

The fact that the extended [C II] haloes surface brightness can be successfully fit by our model does not entail that outflows are the only possible explanation. Other possibilities need to be considered. These include the presence of faint satellite galaxies and disturbed morphologies due to ongoing merger activity. While such alternative scenarios seem plausible, given that mergers and satellites are common features in simulations at high redshift (Kohandel et al. 2019; Gelli et al. 2020), note that Fujimoto et al. (2019) discard galaxies with disturbed morphologies from the sample used in their analysis. Also, the increasing trend of the [C II] luminosity-SFR surface density ratio with radius would imply a non-physical [C II] emissivity in satellites. It is difficult to confirm the dynamical effect of merger/satellites from current observations (Rizzo et al. 2022). Thus, dedicated ALMA observations, such as the ongoing CRISTAL Large Program (PI: Herrera-Camus), can probe the role of outflows and alternative halo formation scenarios either by spatially resolving the presence of satellites and disturbed morphologies, or by finding direct signs of outflows in the [C II] line spectra of halo-hosting systems (Section 6). The *JWST* can also be used to resolve the halo regions in $z \sim 4$ – 6 galaxies and to, e.g. gauge the contribution of satellite galaxies to the total [C II] extended emission (Gelli et al. 2021).

In any case, exploring theoretically multiple scenarios is especially appropriate considering that, despite its success, the model presented here contains several limitations and hypotheses that will need to be further refined in the future. For instance, the assumption of spherical symmetry prevents a thorough study of more realistic haloes morphologies revealed by observations. In the same way, the steady-state approach hinders a careful assessment of the halo evolution under the influence of the dark matter gravitational potential. Gas turbulence and interactions with the external CGM/IGM environment may also

affect the wind evolution and change the density structure of the gas, which is directly connected to the final [C II] emission. Furthermore, non-equilibrium cooling and recombination should also be included, as they can significantly alter the final temperature profiles (Gray et al. 2019; Danehkar, Oey & Gray 2021).

Despite the intrinsic limitations of our model, it is very encouraging to find such a good level of agreement with data within a clear, physically motivated framework. On this basis, we concluded that observed haloes are the likely smoking gun of early CGM enrichment caused by supernova-driven outflows in primordial galaxies.

ACKNOWLEDGEMENTS

We are grateful to Seiji Fujimoto for sharing his study on ALPINE data with us. EP is grateful to Matus Rybak and Kirsty Butler for fruitful discussion. AF, AP, LS, MK, and SC acknowledge support from the ERC Advanced Grant INTERSTELLAR H2020/740120 (PI: Ferrara). Any dissemination of results must indicate that it reflects only the author's view and that the Commission is not responsible for any use that may be made of the information it contains. Partial support from the Carl Friedrich von Siemens-Forschungspreis der Alexander von Humboldt-Stiftung Research Award is kindly acknowledged (AF). We gratefully acknowledge computational resources of the Center for High Performance Computing (CHPC) at SNS. We acknowledge use of the PYTHON programming language (Van Rossum & de Boer 1991), ASTROPY (Astropy Collaboration 2013), EMCEE (Foreman-Mackey et al. 2013), Corner (Foreman-Mackey 2016), MATPLOTLIB (Hunter 2007), NUMPY (van der Walt, Colbert & Varoquaux 2011), and SCIPY (Jones et al. 2001).

DATA AVAILABILITY

The derived data generated in this research will be shared on reasonable requests to the corresponding author.

REFERENCES

- Akins H. et al., 2022, *ApJ*, 934, 64
 Arata S., Yajima H., Nagamine K., Li Y., Khochfar S., 2019, *MNRAS*, 488, 2629
 Asplund M., Grevesse N., Sauval A. J., Scott P., 2009, *ARA&A*, 47, 481
 Astropy Collaboration, 2013, *A&A*, 558, A33
 Bacon R. et al., 2017, *A&A*, 608, A1
 Barchiesi L. et al., 2022, *A&A*, preprint (arXiv:2212.00038)
 Behroozi P. S., Wechsler R. H., Conroy C., 2013, *ApJ*, 770, 57
 Béthermin M. et al., 2020, *A&A*, 643, A2
 Bouwens R. J. et al., 2015, *ApJ*, 803, 34
 Bouwens R. J. et al., 2022, *ApJ*, 931, 160
 Bouwens R., Oesch P., Illingworth G., Ellis R., Stefanon M., 2017, *ApJ*, 843, 129
 Bradley L. D. et al., 2014, *ApJ*, 792, 76
 Brügggen M., Scannapieco E., 2016, *ApJ*, 822, 31
 Calura F. et al., 2021, *MNRAS*, 500, 3083
 Capak P. et al., 2015, *Nature*, 522, 455
 Carniani S. et al., 2018, *MNRAS*, 478, 1170
 Carniani S. et al., 2020, *MNRAS*, 499, 5136
 Chevalier R. A., Clegg A. W., 1985, *Nature*, 317, 44 (CC85)
 Chisholm J. et al., 2018, *A&A*, 616, A30
 da Cunha E. et al., 2013, *ApJ*, 766, 13
 Danehkar A., Oey M. S., Gray W. J., 2021, *ApJ*, 921, 91
 Davé R., Finlator K., Oppenheimer B. D., 2012, *MNRAS*, 421, 98
 Dayal P., Ferrara A., 2018, *Phys. Rept.*, 780-782, 1
 De Looze I. et al., 2014, *A&A*, 568, A62
 Dessauges-Zavadsky M. et al., 2020, *A&A*, 643, A5
 Dutton A. A., Maccio A. V., 2014, *MNRAS*, 441, 3359
 Faisst A. L. et al., 2020, *ApJ*, 247, 61
 Faisst A. L. et al., 2022, *Universe*, 8, 314
 Ferrara A., Vallini L., Pallottini A., Gallerani S., Carniani S., Kohandel M., Decataldo D., Behrens C., 2019, *MNRAS*, 489, 1
 Field G. B., 1958, *Proc. IRE*, 46, 240
 Fielding D. B., Bryan G. L., 2022, *ApJ*, 924, 82
 Finlator K., Dave R., 2008, *MNRAS*, 385, 2181
 Foreman-Mackey D., 2016, *J. Open Source Softw.*, 1, 24
 Foreman-Mackey D., Hogg D. W., Lang D., Goodman J., 2013, *PASP*, 125, 306
 Fudamoto Y. et al., 2022, *ApJ*, 934, 144
 Fujimoto S. et al., 2019, *ApJ*, 887, 107
 Fujimoto S. et al., 2020, *ApJ*, 900, 1 (F20)
 Gallerani S., Pallottini A., Feruglio C., Ferrara A., Maiolino R., Vallini L., Riechers D. A., Pavesi R., 2018, *MNRAS*, 473, 1909
 Gelli V., Salvadori S., Ferrara A., Pallottini A., Carniani S., 2021, *ApJ*, 913, L25
 Gelli V., Salvadori S., Pallottini A., Ferrara A., 2020, *MNRAS*, 498, 4134
 Ginolfi M. et al., 2020, *A&A*, 633, A90
 Gnedin N. Y., Hollon N., 2012, *ApJ*, 202, 13
 Gong Y., Cooray A., Silva M., Santos M. G., Bock J., Bradford C. M., Zemcov M., 2012, *ApJ*, 745, 49
 Goodman J., Weare J., 2010, *Commun. Appl. Math. Comp. Sci.*, 5, 65
 Gray W. J., Oey M., Silich S., Scannapieco E., 2019, *ApJ*, 887, 161
 Gronke M., Oh S. P., 2020, *MNRAS*, 494, L27
 Harikane Y. et al., 2022, *ApJ*, 929, 1
 Hashimoto T. et al., 2018, *Nature*, 557, 392
 Hastings W. K., 1970, *Biometrika*, 57, 97
 Heckman T. M., Alexandroff R. M., Borthakur S., Overzier R., Leitherer C., 2015, *ApJ*, 809, 147
 Herrera-Camus R. et al., 2015, *ApJ*, 800, 1
 Herrera-Camus R. et al., 2018, *ApJ*, 861, 95
 Herrera-Camus R. et al., 2021, *A&A*, 649, A31
 Hodge J. A., da Cunha E., 2020, *Roy. Soc. Open Sci.*, 7, 200556
 Hollenbach D. J., Tielens A. G. G. M., 1999, *Rev. Modern Phys.*, 71, 173
 Hopkins P. F. et al., 2018, *MNRAS*, 480, 800
 Hopkins P. F., Kereš D., Oñorbe J., Faucher-Giguère C.-A., Quataert E., Murray N., Bullock J. S., 2014, *MNRAS*, 445, 581
 Hunter J. D., 2007, *Comp. Sci. Eng.*, 9, 90
 Jones E. et al., 2001, *SciPy: Open Source Scientific Tools for Python*. Available at: <http://www.scipy.org/>
 Katz H. et al., 2021, *MNRAS*, 507, 1254
 Kawamata R., Ishigaki M., Shimasaku K., Oguri M., Ouchi M., Tanigawa S., 2018, *ApJ*, 855, 4
 Kohandel M., Pallottini A., Ferrara A., Zanella A., Behrens C., Carniani S., Gallerani S., Vallini L., 2019, *MNRAS*, 487, 3007
 Le Fèvre O. et al., 2020, *A&A*, 643, A1
 Livermore R. C., Finkelstein S. L., Lotz J. M., 2017, *ApJ*, 835, 113
 Ma X., Quataert E., Wetzel A., Hopkins P. F., Faucher-Giguère C.-A., Kereš D., 2020, *MNRAS*, 498, 2001
 Maiolino R. et al., 2015, *MNRAS*, 452, 54
 Mannucci F., Salvaterra R., Campisi M. A., 2011, *MNRAS*, 414, 1263
 Matthee J. et al., 2017, *ApJ*, 851, 145
 McCourt M., O'Leary R. M., Madigan A.-M., Quataert E., 2015, *MNRAS*, 449, 2
 McCourt M., Oh S. P., O'Leary R., Madigan A.-M., 2018, *MNRAS*, 473, 5407
 Metropolis N., Rosenbluth A. W., Rosenbluth M. N., Teller A. H., Teller E., 1953, *J. Chem. Phys.*, 21, 1087
 Muratov A. L., Kereš D., Faucher-Giguère C.-A., Hopkins P. F., Quataert E., Murray N., 2015, *MNRAS*, 454, 2691
 Navarro J. F., Frenk C. S., White S. D. M., 1997, *ApJ*, 490, 493
 Nelson D. et al., 2019, *MNRAS*, 490, 3234
 Oesch P. A. et al., 2012, *ApJ*, 745, 110
 Oesch P. A. et al., 2016, *ApJ*, 819, 129
 Oesch P. et al., 2009, *ApJ*, 709, L21

Olsen K., Greve T. R., Narayanan D., Thompson R., Davé R., Niebla Rios L., Stawinski S., 2017, *ApJ*, 846, 105
 Pallottini A. et al., 2019, *MNRAS*, 487, 1689
 Pallottini A. et al., 2022, *MNRAS*, 513, 5621
 Pallottini A., Ferrara A., Bovino S., Vallini L., Gallerani S., Maiolino R., Salvadori S., 2017b, *MNRAS*, 471, 4128
 Pallottini A., Ferrara A., Gallerani S., Salvadori S., D’Odorico V., 2014, *MNRAS*, 440, 2498
 Pallottini A., Ferrara A., Gallerani S., Vallini L., Maiolino R., Salvadori S., 2017a, *MNRAS*, 465, 2540
 Pallottini A., Gallerani S., Ferrara A., Yue B., Vallini L., Maiolino R., Feruglio C., 2015, *MNRAS*, 453, 1898
 Pentericci L. et al., 2016, *ApJ*, 829, L11
 Pizzati E., Ferrara A., Pallottini A., Gallerani S., Vallini L., Decataldo D., Fujimoto S., 2020, *MNRAS*, 495, 160 (P20)
 Rizzo F., Kohandel M., Pallottini A., Zanella A., Ferrara A., Vallini L., Toft S., 2022, *A&A*, 667, A5
 Rupke D. S., 2018, *Galaxies*, 6, 138
 Rybak M., Hodge J. A., Vegetti S., van der Werf P., Andreani P., Graziani L., McKean J. P., 2019, *MNRAS*, 494, 5542
 Sarkar K. C., Nath B. B., Sharma P., 2015, *MNRAS*, 453, 3827
 Scannapieco E., 2017, *ApJ*, 837, 28
 Scannapieco E., Brüggem M., 2015, *ApJ*, 805, 158
 Schaerer D. et al., 2020, *A&A*, 643, A3
 Schneider E. E., Robertson B. E., 2017, *ApJ*, 834, 144
 Schneider E. E., Robertson B. E., Thompson T. A., 2018, *ApJ*, 862, 56
 Sharma S., 2017, *ARA&A*, 55, 213
 Shibuya T., Ouchi M., Harikane Y., 2015, *ApJS*, 219, 15
 Spilker J. S. et al., 2020, *ApJ*, 905, 86
 Stacey G. J., Townes C. H., Poglitsch A., Madden S. C., Jackson J. M., Herrmann F., Genzel R., Geis N., 1991, *ApJ*, 382, L37
 Stern J. et al., 2021, *MNRAS*, 507, 2869
 Strickland D. K., Heckman T. M., 2009, *ApJ*, 697, 2030
 Thompson T. A., Quataert E., Zhang D., Weinberg D. H., 2016, *MNRAS*, 455, 1830
 Vallini L., Ferrara A., Pallottini A., Carniani S., Gallerani S., 2021, *MNRAS*, 505, 5543
 Vallini L., Gallerani S., Ferrara A., Pallottini A., Yue B., 2015, *ApJ*, 813, 36
 van der Walt S., Colbert S. C., Varoquaux G., 2011, *Comp. Sci. Eng.*, 13, 22
 Van Rossum G., de Boer J., 1991, *CWI Quarterly*, 4, 283
 Vogelsberger M., Marinacci F., Torrey P., Puchwein E., 2020, *Nat. Rev. Phys.*, 2, 42
 Wise J. H., Demchenko V. G., Halicek M. T., Norman M. L., Turk M. J., Abel T., Smith B. D., 2014, *MNRAS*, 442, 2560
 Wolfire M. G., McKee C. F., Hollenbach D., Tielens A. G. G. M., 2003, *ApJ*, 587, 278
 Xu H., Wise J. H., Norman M. L., Ahn K., O’Shea B. W., 2016, *ApJ*, 833, 84
 Zhang H. et al., 2021, *ApJ*, 916, 101

APPENDIX A: DETAILS ON THE CMB SUPPRESSION

We study the effects of CMB photons on the C II level populations. Specifically, we focus on the levels that give rise to the [C II] 158 μm ($^2P_{3/2} \rightarrow ^2P_{1/2}$). We consider these two levels as a closed system, and, assuming statistical equilibrium, we write the balance equation for these two levels as (Gong et al. 2012; da Cunha et al. 2013)

$$n_l(n_e \gamma_{lu} + B_{lu} I(\nu)) + P_{lu}^{(\text{UV})} = n_u(n_e \gamma_{ul} + A_{ul} + B_{ul} I(\nu)) + P_{ul}^{(\text{UV})}. \quad (\text{A1})$$

In this relation, n_l and n_u are the numeric densities of the two levels, and n_e is the density of free electrons, i.e. the main collisional partners for [C II] in the range of densities we are interested in (Vallini et al. 2015). A_{ul} , $B_{ul, lu}$, the Einstein coefficients, $\gamma_{ul, lu}$ the collisional excitation rates, and $I(\nu) = B(\nu, z)$ is the (black-body) specific intensity of the CMB radiation.

Finally, $P_{ul, lu}^{(\text{UV})}$ are UV excitation and de-excitation rates. These account for the UV pumping effect: in the presence of FUV radiation at 1330 \AA , electrons can be pumped from the $^2P_{3/2}$ ($^2P_{1/2}$) level to $^2D_{3/2}$ at 1335.66 \AA (1334.53 \AA). This can lead to the [C II] fine structure transitions $^2D_{3/2} \rightarrow ^2P_{3/2} \rightarrow ^2P_{1/2}$, resulting in a mixing of the levels of the C II doublet. The UV rates parametrize this effect in the context of a two-level treatment, and are given by the following expressions (Field 1958):

$$P_{ul}^{(\text{UV})} = \frac{g_k}{g_u} \frac{A_{kl} A_{ku}}{A_{kl} + A_{ku}} \left(\frac{c^2 I_{\text{UV}}(\nu_{ku})}{2h\nu_{ku}^3} \right), \quad (\text{A2})$$

$$P_{lu}^{(\text{UV})} = \frac{g_k}{g_l} \frac{A_{kl} A_{ku}}{A_{kl} + A_{ku}} \left(\frac{c^2 I_{\text{UV}}(\nu_{kl})}{2h\nu_{kl}^3} \right), \quad (\text{A3})$$

where I_{UV} is the UV radiation intensity, and k is the level $^2D_{3/2}$, which has degeneracy $g_k = 4$; $A_{kl} = 2.41 \times 10^8 \text{ s}^{-1}$ (ν_{kl}) and $A_{ku} = 4.76 \times 10^7 \text{ s}^{-1}$ (ν_{ku}) are the Einstein coefficients (frequencies) of the $^2D_{3/2} \rightarrow ^2P_{1/2}$ and $^2D_{3/2} \rightarrow ^2P_{3/2}$ transitions, respectively.

The ratio between the UV rates determines the UV colour temperature, defined as (for the case of interest, $T_{\text{UV}} \approx 10^4 \text{ K}$)

$$T_{\text{UV}} = T_* \log \left(\frac{g_u P_{ul}^{(\text{UV})}}{g_l P_{lu}^{(\text{UV})}} \right), \quad (\text{A4})$$

where $T_* \approx 91 \text{ K}$ is the equivalent temperature of the C II transition.

It is also convenient to introduce the excitation temperature of the transition, which is defined in a similar way:

$$T_{\text{exc}} = T_* \log \left(\frac{g_u n_l}{g_l n_u} \right). \quad (\text{A5})$$

Using the relations linking the three Einstein coefficients, and the two collisional excitation rates, we can rewrite equation A1 and obtain the following expression for T_{exc} :

$$\frac{T_*}{T_{\text{exc}}} = \log \left(\frac{A_{ul} (1 + c^2 I(\nu_*)/2h\nu_*^3) + n_e \gamma_{ul} + P_{ul}^{(\text{UV})}}{A_{ul} c^2 I(\nu_*)/2h\nu_*^3 + n_e \gamma_{ul} e^{-T_*/T} + P_{lu}^{(\text{UV})}} \right). \quad (\text{A6})$$

Once T_{exc} is known, it is possible to compute the CMB suppression factor according to equation 6 (Section 2.2).

APPENDIX B: DETAILS ON THE MODEL-DATA COMPARISON

To compare our model with data, we adopt a Bayesian framework, i.e. we compute the likelihood and posterior distributions. The former quantifies the model-data agreement; the latter determines the best-fit values of the model parameters.

We denote the parameter set with Θ , and our model with $m(b; \Theta)$, where b is the impact parameter of the surface brightness profiles. We consider as parameters (a) the mass loading factor η , (b) the SFR, and (c) the circular velocity V_c . In principle, the redshift, z , is another parameter. However, for our sample high-quality spectroscopic redshifts are available (Table 1). Hence, we set $z = z_{\text{C II}}$, and limit our parameter space to $\Theta = (\eta, \text{SFR}, V_c)$.

The likelihood of a set of n data points $d = \{y_i(b_i) \pm \sigma_i\}$ is

$$\mathcal{L}(d | \Theta, m) = \exp \left(- \sum_{i=1}^n \frac{(y_i - m(b_i; \Theta))^2}{\sigma_i^2} \right). \quad (\text{B1})$$

The posterior can be expressed in terms of the likelihood and the prior distributions. Our *a-priori* knowledge of the parameters varies. The mass loading factor is largely unconstrained both theoretically and observationally; even its order of magnitude is quite uncertain, ranging from $\eta \lesssim 0.1$ to $\eta \gtrsim 10$ (e.g. Muratov et al. 2015). For this

reason, the most suitable prior for η is a logarithmic prior (i.e. a uniform prior for $\log \eta$). Therefore, from now on we work with the parameter $\log \eta$, assigning to it a uniform distribution in $-1 < \log \eta < 1.5$.

On the other hand, both the SFR and V_c are somewhat constrained by the ancillary data reported in Table 1. In principle, we could set these parameters to the median values inferred from observations. However, the inferred SFRs and virial masses are relatively uncertain (errors $\lesssim 50$ per cent). Given that our model turns out to be sensitive to relatively small changes in these parameters, we include them in the analysis, using the information we have from observations to set the priors properly. Given that the uncertainties of SFR and V_c are roughly symmetric in logarithmic space, we choose lognormal priors for both of these quantities. The mean of the distribution is taken to be equal to the (logarithm of) their measured values, and the standard deviation is set to half of the total (upper + lower) relative uncertainty on these values.

Overall, the prior distribution we consider is null outside the region $-1 < \log \eta < 1.5$; inside this region it is proportional to

$$\pi(\Theta|m) \propto \exp \left(- \frac{(\log_{10} \text{SFR} - \log_{10} \text{SFR}_i)^2}{2\sigma_{\log, \text{SFR}, i}^2} - \frac{(\log_{10} V_c - \log_{10} V_{c,i})^2}{2\sigma_{\log, V_c, i}^2} \right), \quad (\text{B2})$$

where $\log_{10} \text{SFR}_i \pm \sigma_{\log, \text{SFR}, i}$, and $\log_{10} V_{c,i} \pm \sigma_{\log, V_c, i}$ refer to the values displayed in Table 1.

Once the priors are set, the posterior distribution is well-defined, and it can be explored with a sampling algorithm such as an MCMC (Metropolis et al. 1953; Hastings 1970). Here, we use the well-known code EMCEE (Foreman-Mackey et al. 2013) to run an MCMC using the affine-invariant ensemble prescription to generate new samples (Goodman & Weare 2010). For each system considered (Table 1), we run the MCMC algorithm by placing $m = 48$ walkers distributed randomly in the parameter space and evolving them for $N > 10^5$ steps. We set the final number of steps so that our chain is at least 100 times longer than the autocorrelation time τ (see e.g. Sharma 2017). This is easily achieved for the unimodal posteriors in Fig. C1, while it takes longer integration times for some of the systems showing a bi-modal behavior (i.e. DC630594, DC689613, and DC881725). As the final chain is produced, we discard the first $k > 10^3$ elements to account for the burn-in phase, and we thin the chain considering only one element every τ steps in order to account for autocorrelations.

APPENDIX C: RESULTS FOR THE WHOLE SAMPLE

In Fig. C1, we show the posterior distributions for all the systems considered in Table 1 with the exception of DC396844, which is discussed at length in the main text (see Fig. 3).

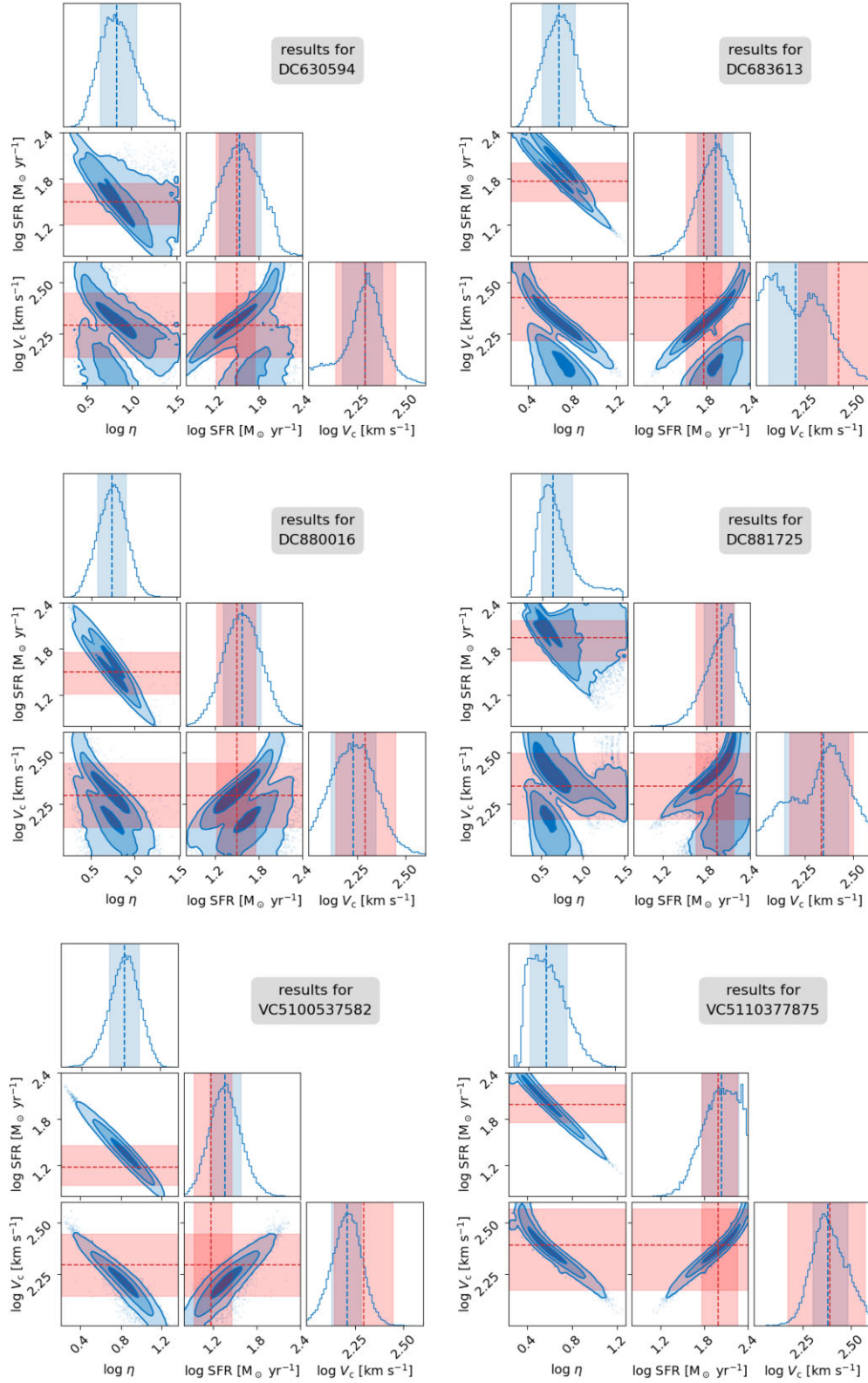


Figure C1. Corner plots for all the systems but DC396844 (shown in the main text). Details can be found in Fig. 3 (left-hand panel).

This paper has been typeset from a $\text{\TeX}/\text{\LaTeX}$ file prepared by the author.